Scanning Tunneling Microscopy Observation of an Electronic Superlattice at the Surface of Clean Gold

W. Chen, V. Madhavan, T. Jamneala, and M. F. Crommie
Department of Physics, Boston University, 590 Commonwealth Avenue, Boston, Massachusetts 02215
(Received 18 August 1997)

We have used scanning tunneling spectroscopy to spatially resolve the electronic structure of clean Au(111) at low temperature. We find that the long-range herringbone reconstruction on Au(111) acts as a superlattice for surface-state electrons, creating a new band structure and modulated electronic density. Low energy electrons respond to the superlattice by localizing in the hexagonal-close-packed (hcp) region of the reconstruction, while higher energy electrons reverse this trend, shifting density back to the adjacent face-centered-cubic (fcc) region. These observations are quantitatively explained by an extended Kronig-Penney model, from which we estimate the well-depth of the reconstruction-induced surface superlattice. [S0031-9007(97)05182-X]

PACS numbers: 68.35.Bs, 61.16.Ch, 73.20.At

When a superlattice is imposed on a periodic electronic potential, the resultant energy bands are folded back into a reduced Brillouin zone [1]. Local changes in electronic state density, however, must also accompany superlattice formation. A class of systems in which superlattice-induced charge rearrangement should play a role are the reconstructions that often decorate clean metal surfaces [2]. Au(111) has one of the most elaborate of these reconstructions, displaying a surface superstructure with a repeat distance of 23 surface lattice constants (the "herringbone" reconstruction) [3]. The existence of a two-dimensional surface-state band at the Au(111) surface [4] suggests that the reconstruction there should act as a superlattice on surface band structure. Despite numerous photoemission [5,6] and scanning tunneling microscopy (STM) studies [7–10], however, there has so far been no quantitative agreement between clean Au(111) data and superlattice models. Other superlattice systems, such as periodic adsorbate [11] and step arrays [12], have shown signs of band folding in photoemission, but little has been done to *locally* investigate the electronic structure of surface superlattices on metals.

Here, we report the direct observation of electronic superlattice behavior on the reconstructed surface of clean Au(111). Using scanning tunneling spectroscopy, we have observed the spatial and energetic rearrangement of two-dimensional surface-state electrons in response to the long-period superstructure of the herringbone reconstruction. We find that the observed behavior is inconsistent with a localized surface-state picture, but is well explained by the existence of an extended, weakly attractive potential felt by electrons in one-half of the reconstruction unit cell [the hexagonal-close-packed (hcp) region] relative to the other half [the face-centered-cubic (fcc) region]. The resultant two-dimensional band structure of this surface superlattice leads to the opening of energy gaps and a modulated electronic density. By quantitatively comparing our STM data to an extended (2D) Kronig-Penney [1,13] model, we estimate that the electronic potential energy difference between the fcc and hcp regions of the reconstruction is 25 ± 5 meV. We suggest that the physical origin of this potential offset arises from variations in local atomic concentration in the reconstruction unit cell.

The experiments were performed using a home-built STM contained in ultrahigh vacuum and cooled to 4 K. The single-crystal Au sample was prepared by repeated cycles of Ar ion sputtering and annealing before being placed into the STM and cooled to 4 K. The convention used here is that the bias across the tunnel junction (V) is the voltage of the sample measured with respect to the tip. The dI/dV spectra were measured through lock-in detection of the ac tunnel current driven by a 450 Hz, 7 mV (rms) signal added to the junction bias.

Figure 1 shows a constant-current image of a typical 800 Å $\times$ 800 Å patch of the Au(111) surface at 4 K. In addition to monatomic steps, a prominent feature of the surface is a series of parallel zigzag ridges, the well-known $23 \times \sqrt{3}$ herringbone reconstruction [3]. This pattern is formed by a stress-induced surface contraction along the $[1\bar{1}0]$ direction (the line perpendicular to the ridges) [14,15]. In one-half of the reconstruction unit cell, the surface atoms occupy hcp sites, while in the adjacent half, they occupy fcc sites (the hcp region has a width of 25 Å and is noticeably narrower than the 38 Å wide fcc region). The ridges are formed by surface atoms occupying bridge sites between the fcc and hcp regions. A longer range structure, consisting of rotated uniaxial domains, arises to further release surface stress [16,17].

Coexisting with the reconstruction is a series of wave fronts running parallel to step edges on the surface. These standing waves are due to the quantum interference of 2D surface-state electrons scattering off step edges [9,18]. Measurement of the energy dependence of the wavelength of this interference pattern allows one to extract the surface-state dispersion relation [9,18]. We have performed this procedure at 4 K and find that the Au(111) surface-state dispersion is parabolic, with an effective mass ratio of 0.26 and a band edge 0.52 eV below the Fermi

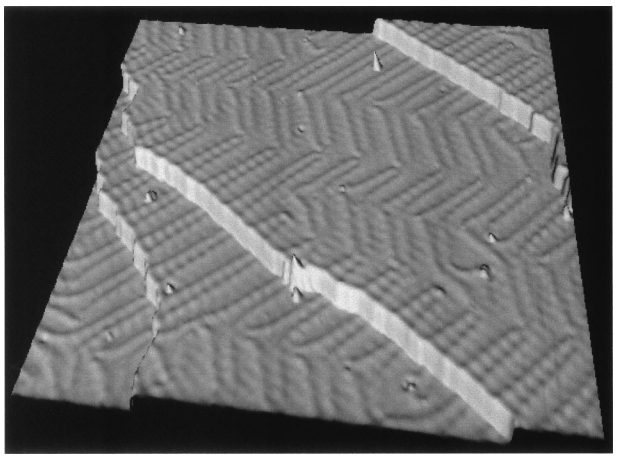

FIG. 1. Constant current 800 Å × 800 Å image of the Au(111) surface at 4 K ($I = 0.5$ nA, $V = 0.01$ V). The herringbone reconstruction and surface-state standing waves are clearly visible. Monatomic steps separating terraces are 2.4 Å high.

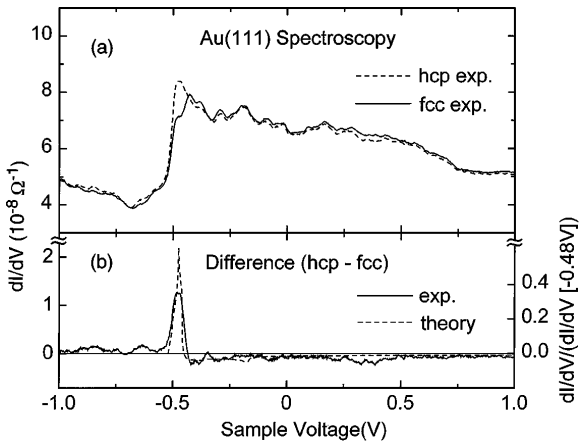

FIG. 2. (a) Average dI/dV spectra taken with the STM tip held over the hcp region and the fcc region of the Au(111) reconstruction. (b) Difference of hcp and fcc spectra shown in (a). Dashed line shows fit to data using extended Kronig-Penney model.

energy (E_F). These results differ from previous room temperature STM results [9], but are in agreement with photoemission results [6].

In order to study how the herringbone reconstruction influences the electronic properties of Au(111), we performed STM spectroscopy in the hcp and fcc regions of the reconstruction unit cell. The dI/dV spectra were measured by first fixing the tip height with tunneling parameters $I = 0.5$ nA, $V = 1.0$ V, and then ramping the bias from 1.0 to -1.0 V while keeping the STM tip stationary (i.e., with the feedback loop opened). Figure 2(a) shows the results of measuring dI/dV spectra at 17 different spots on the gold surface. At each spot, a spectrum was recorded over the middle of both an fcc region of the reconstruction and a nearby hcp region. Spectra from the two regions were separately averaged before plotting.

As seen in Fig. 2(a), both regions of the reconstruction show a nearly identical dropoff in dI/dV as the bias is lowered through the surface-state band edge at -0.52 V. Just above the band edge, however, there is a striking difference between the two regions. Here, the hcp spectrum shows a steep enhancement, while the fcc spectrum is depressed. This behavior is best seen in the difference spectrum (hcp − fcc) plotted in Fig. 2(b). The difference shows up as a peak centered at -0.48 V, having a width of 0.07 V (FWHM). A distinct "crossover" occurs at -0.43 V, as the fcc spectrum rises over the hcp spectrum above this energy, causing the difference to dip below zero. The spatial dependence of the band-edge disparity between the hcp and the fcc regions can be more clearly seen in the spectroscopic map of Fig. 3. Figure 3(a) shows a 400 Å × 400 Å constant current topograph which includes several regular hcp and fcc regions. Figure 3(b) shows a dI/dV map taken at constant dc current over the very same region, with junction bias fixed at -0.48 V (the center of the difference peak). The hcp regions show up much brighter than the fcc regions in the dI/dV map, even though they have roughly equivalent height in the topographic map. Similar contrast between the fcc and hcp regions of the Au(111) reconstruction was seen in the room temperature images of Everson *et al.* [8].

The dI/dV spectroscopy of Figs. 2 and 3 can be interpreted by noting that STM spectroscopy corresponds to a convolution of the tip and surface local density of states (LDOS) [19]. If the same STM tip is used to measure dI/dV at different points on a surface, then differences in dI/dV must arise from differences in the surface LDOS. This allows one to interpret the difference spectrum in Fig. 2(b) as representative of the difference in electronic LDOS between the hcp and fcc regions of the reconstruction. The peak in dI/dV near the band edge thus reveals a tendency for low energy surface-state electrons to localize in the hcp region of the Au(111) reconstruction. This is best seen in Fig. 3(b), where the electronic state density 0.48 eV below E_F is clearly enhanced in the hcp region (see Fig. 3 insets). The crossover at -0.43 V in Fig. 2, however, marks a reversal of this trend, as higher energy electrons tend to favor the fcc region.

These experimental results can be quantitatively explained by the simple ansatz that delocalized surface-state electrons experience a weakly attractive potential in the hcp regions of the reconstruction compared to the fcc regions. We model the potential seen by a 2D surface-state electron on Au(111) as an extended square-well Kronig-Penney (KP) potential [1,13] having the same periodicity as the reconstruction. As shown in the inset of Fig. 4(a), this potential is periodic in the $[1\bar{1}0]$ surface direction (the "x direction," perpendicular to the ridges) but constant in the $[11\bar{2}]$ direction (the "y direction," parallel to the ridges). Domain rotation is ignored in this simple model. In order to compare the model to our STM data, we calculate the electronic LDOS of the extended KP potential. The eigenstates can be written as

$$\Psi_{k_x k_y}(x, y) = e^{ik_y y} e^{ik_x x} u_{k_x}(x),$$

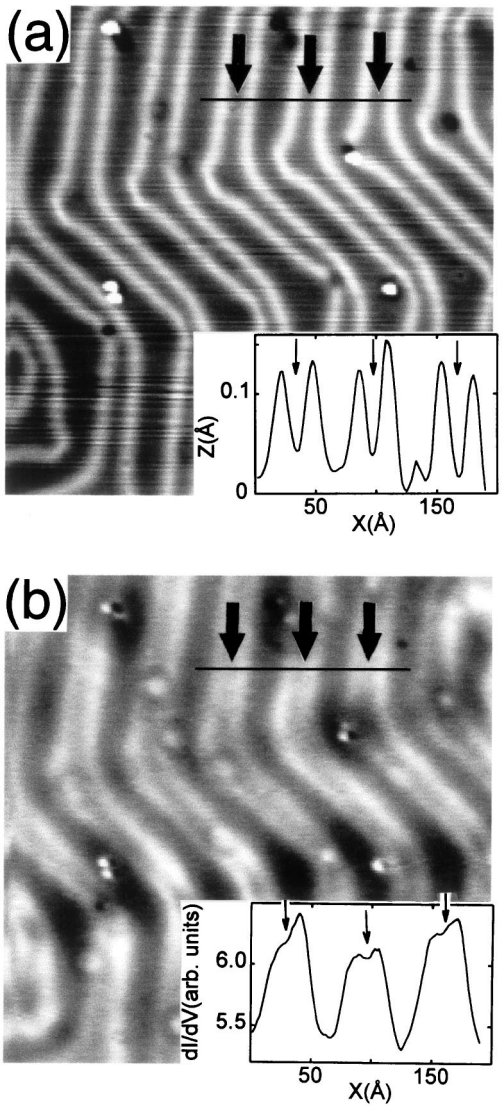

FIG. 3. (a) Constant current 400 Å × 400 Å image of Au(111) surface ($I = 1$ nA, $V = -0.48$ V). Inset shows height line scan across three unit cells of reconstruction. Arrows point to hcp regions. (b) Constant dc current dI/dV map at $V = -0.48$ V for the same region shown in (a) ($I_{\mathrm{dc}} = 1.2$ nA). Inset shows dI/dV intensity line scan across the same three unit cells as in (a). Arrows point to hcp regions.

where $u_{k_x}(x)$ is periodic, as ensured by the Bloch theorem [1]: $u_{k_x}(x + a + b) = u_{k_x}(x)$ (here $a = 25$ Å represents the width of the hcp region, or "trough" of the periodic square well, and $b = 38$ Å represents the width of the fcc region, or "crest" of the periodic well). The eigenstates are obtained by matching $\Psi_{k_x k_y}(x, y)$ at the boundaries $x = a$ and $x = a + b$ [1], after which the LDOS can be found by evaluating the following expression [13]:

$$\mathrm{LDOS}(E, x, y) = \frac{a + b}{\pi^2}\sqrt{\frac{2m^*}{\hbar^2}} \times \int_0^{k'} dk_x \, |\Psi_{k_x k_y}(x, y)|^2 \, \frac{1}{\sqrt{E - \varepsilon(k_x)}}.$$

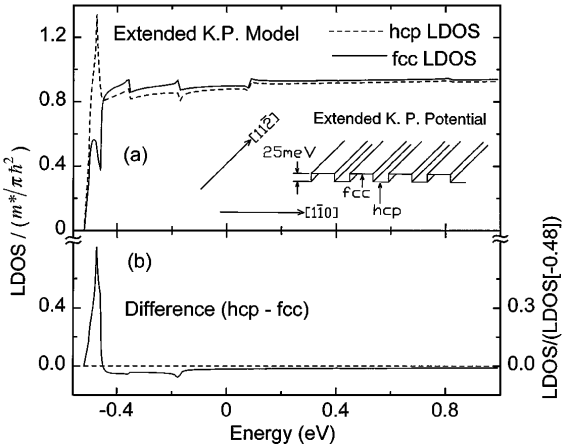

FIG. 4. (a) Theoretical LDOS calculated at the centers of the hcp and fcc regions of the extended Kronig-Penney potential. The inset shows a sketch of the potential. (b) Difference of theoretical LDOS curves shown in (a).

Here, $\varepsilon(k_x)$ is the 1D KP dispersion along $[1\bar{1}0]$, $k' = \sqrt{\frac{2m^*E}{\hbar^2}}$, and $m^* = 0.26m_e$ is the effective mass of a surface-state electron (m_e is the bare electron mass). To compare with experimental data, the energy zero of the calculation (i.e., the lowest eigenstate energy) is taken to coincide with the experimental band edge 0.52 eV below E_F.

Figure 4(a) shows the theoretical LDOS calculated at the centers of both the hcp and fcc regions of the extended KP potential. The only free parameter in the model is the depth of the square-well potential, here taken as 25 meV. As with any periodic potential, the extended KP potential leads to a band structure that includes energy gaps. These can be seen as sharp kinks in both curves, and occur at energies corresponding to the Brillouin zone boundaries of the KP superlattice. The LDOS does not go to zero at these energies because of the free-particle motion in the $[11\bar{2}]$ direction [i.e., new gaps open up along the $\overline{\Gamma K}$ line, but not along the $\overline{\Gamma M}$ line in the Au(111) surface Brillouin zone]. The most striking feature of the theoretical curves occurs at low energy, where a large peak in the hcp LDOS dominates over a much reduced fcc peak. This is the same behavior seen in the experimental curves of Fig. 2(a), and is due to the "bound state" nature of eigenstates whose energy lies below the top of the square-well potential. These states are exponentially damped in the barrier region (i.e., the fcc region), and, thus, are highly localized in the hcp region. At slightly higher energy, however, the eigenstate energy rises above the top of the square wells into the "continuum" regime. In this regime, the propagating electrons "slow down" over the barrier regions; hence, the fcc (barrier region) state density rises above the hcp curve at higher energy. This explains the crossover seen in the data at $V = -0.43$ V (Fig. 2). At extremely high energies, the influence of the potential becomes less important and the LDOS approaches the 2D free electron limit of $m^*/\pi\hbar^2$ for both regions.

The calculated LDOS for the hcp and fcc regions was quantitatively compared to experimental results by taking the difference between the theoretical curves of Fig. 4(a) and fitting it to our spectroscopic data. To remove unknown scale factors, both the theoretical and experimental curves were normalized by the relative height of their respective peaks at -0.48 V in the hcp region. Figure 2(b) shows a direct comparison of theory to experiment for a well depth of 25 meV (the well depth is the only fitting parameter). The fit is compelling, as the extended KP model faithfully reproduces both the experimental low energy peak and higher energy crossover regime. (Varying the well depth by 5 meV in either direction leads to a visibly degraded fit.) The low energy experimental peak corresponds to the first "kink" in the theoretical LDOS curve, and, thus, directly reflects the opening of the first reconstruction-induced energy gap along the $\overline{\Gamma K}$ line of the reduced surface Brillouin zone of Au(111). The higher energy gap features, however, cannot be seen in the data. This discrepancy, along with the extra rounding of the experimental peak, might be explained by a combination of surface defects, reconstruction domain formation, and experimental noise.

To summarize, the spatially varying electronic structure we observe on clean Au(111) is well described by a reconstruction-induced electronic superlattice and subsequent new band structure. While the actual potential landscape is surely more complicated than the periodic square well we have assumed, this work gives strong evidence that the hcp region of the reconstruction provides a broad, shallow electronic well that is approximately 25 meV deeper than the fcc region. The physical origin of this potential offset might be due to the slightly higher concentration of atoms in the hcp region when buried layers are taken into account. Au atoms have a very attractive pseudopotential for s electrons, implying that regions of higher Au concentration should also be regions of lower overall potential for electrons in the sp-derived surface-state band [20]. This situation is in contrast to the clean Si(111)-(7×7) surface, where surface-state electronic behavior is dominated by the more localized nature of dangling bonds [21]. For localized dangling bonds, geometric variation in a reconstruction can be expected to result in *energetic shifting* of spectroscopic peaks measured over different surface regions. This behavior, however, is not observed on pristine Au(111), where delocalized surface electrons respond mainly to the reconstruction by spatially transferring state density at *one particular energy* (i.e., at the energy corresponding to the first Brillouin zone boundary of the surface superlattice).

It is natural to ask why other techniques, such as angle resolved photoemission, have not seen the effects of this superlattice. The most probable reason is that the low superlattice potential leads to extremely small band gaps (less than 20 meV) and low mixing of higher order reciprocal lattice vector terms in the electronic eigenstates. This greatly reduces the probability of observing band-folding effects with photoemission. In conclusion, we suggest that similar superlattice effects might play a role in the electronic properties of other clean, reconstructed metal surfaces [2], as well as thin metal overlayers where lattice mismatch leads to long-period superlattice structures [22].

We gratefully acknowledge E. Jensen and M. El-Batanouny for useful discussions, and J. Cumings for technical support. This work was supported by NSF DMR-9457955, NSF DMR-9503837, the W. M. Keck Foundation, and the George I. Alden Trust.

[1] C. Kittel, *Introduction to Solid State Physics* (Wiley, New York, 1986).
[2] S. Titmuss *et al.*, Chem. Rev. **96**, 1291 (1996).
[3] J. Perdereau *et al.*, J. Phys. F, Met. Phys. **4**, 798 (1974); M. A. v. Hove *et al.*, Surf. Sci. **103**, 189 (1981); H. Melle and E. Menzel, Z. Naturforsch. A **33**, 282 (1978); K. Takayanagi and K. Yagi, Trans. Jpn. Inst. Met. **24**, 337 (1983); U. Harten *et al.*, Phys. Rev. Lett. **54**, 2619 (1985); K. G. Huang *et al.*, Phys. Rev. Lett. **65**, 3313 (1990); Ch. Woll *et al.*, Phys. Rev. B **39**, 7988 (1989); J. V. Barth *et al.*, Phys. Rev. B **42**, 9307 (1990); D. D. Chambliss *et al.*, Phys. Rev. Lett. **66**, 1721 (1991).
[4] P. Heimann and H. J. Neddermeyer, J. Phys. F, Met. Phys. **7**, L37 (1977).
[5] S. D. Kevan and R. H. Gaylord, Phys. Rev. B **36**, 5809 (1987).
[6] S. LaShell, B. A. McDougall, and E. Jensen, Phys. Rev. Lett. **77**, 3419 (1996).
[7] W. J. Kaiser and R. C. Jaklevic, IBM J. Res. Dev. **30**, 411 (1986).
[8] M. P. Everson, R. C. Jaklevic, and W. Shen, J. Vac. Sci. Technol. A **8**, 3662 (1990).
[9] Y. Hasegawa and P. Avouris, Phys. Rev. Lett. **71**, 1071 (1993).
[10] D. Fujita *et al.*, Phys. Rev. Lett. **78**, 3904 (1997).
[11] A. Goldman, in *Angle Resolved Photoemission*, edited by S. D. Kevan (Elsevier, New York, 1992), p. 291.
[12] X. Y. Wang *et al.*, Phys. Rev. B **53**, 15 738 (1996).
[13] L. C. Davis *et al.*, Phys. Rev. B **43**, 3821 (1991).
[14] M. El-Batanouny *et al.*, Phys. Rev. Lett. **58**, 2762 (1987).
[15] N. Takeuchi, C. T. Chan, and K. M. Ho, Phys. Rev. B **43**, 13 899 (1991).
[16] S. Narasimhan and D. Vanderbilt, Phys. Rev. Lett. **69**, 1564 (1992).
[17] R. Ravelo and M. El-Batanouny, Phys. Rev. B **47**, 12 771 (1993).
[18] M. F. Crommie, C. P. Lutz, and D. M. Eigler, Nature (London) **363**, 524 (1993).
[19] J. Tersoff and D. R. Hamann, Phys. Rev. B **31**, 805 (1985).
[20] V. Heine and L. D. Marks, Surf. Sci. **165**, 65 (1986).
[21] J. A. Kubby *et al.*, Phys. Rev. B **43**, 9346 (1991).
[22] C. Guenther *et al.*, Phys. Rev. Lett. **74**, 754 (1995).